Transcranial ultrasound of cerebral vessels *in silico*: proof of concept

Yu. V. Vassilevski*[†], K. A. Beklemysheva[†], G. K. Grigoriev[‡], A. O. Kazakov[†], N. S. Kulberg[§], I. B. Petrov[†], V. Yu. Salamatova*[†], and A. V. Vasyukov[†]

Abstract — Correct diagnostics of vascular pathologies underlies treatment success for patients with cerebrovascular diseases. Transcranial ultrasound is the well-known method for diagnostic of cerebrovascular diseases. Despite high sensitivity and specificity of the method, transcranial ultrasound has some limitations related to the B-mode image quality and accurate insonation of vessels of interest. Overcoming these limitations enables to enhance the quality of the diagnostic procedure. The present work addresses the numerical simulation of ultrasound propagation in a human head by a grid-characteristic method. We used a human tissue-mimicking phantom to verify our numerical model in terms of the accuracy of distance estimation. We obtained pressure distributions within a 3D segmented model of a human head. Our pilot study has some limitations, nevertheless the simulation results demonstrate that mathematical modelling of the transcranial ultrasound can be an effective tool to enhance the ultrasound examination.

Keywords: Transcranial ultrasound, mathematical modelling, grid-characteristic method.

MSC 2010: 65A01, 65B02

Ultrasonography is one of the most reliable and accessible diagnostic procedures due to its low cost, informative value and safety. The result of ultrasound examination is often the deciding factor in the diagnosis and in the choice of treatment methods. Several modes of ultrasound scanning are used conventionally [2]. The most frequently used mode in medical diagnostic examination is the B-mode (brightness mode) which represents two-dimensional image of ultrasound echoes. Intensity of the echo is characterized by the brightness of the spot, and the position of the echo is determined from the position of the transducer and the transit time of the acoustic pulse. The B-mode imaging allows us to visualize and to study morphological condition of different internal anatomical structures in real time.

*Institute of Numerical Mathematics of the RAS, Moscow 119333, Russia.

[†]Moscow Institute of Physics and Technology, Dolgoprudny 141700, Moscow Region, Russia. E-mail: yuri.vassilevski@gmail.com

[‡]MGTS Medical and health center, Petrovsky blvd., 12, bld. 1, Moscow 127051, Russia

[§]Moscow Scientific and Practical Center of Medical Radiology, Srednaya Kalitnikovskaya street, 28, bld. 1, Moscow 109029, Russia. Institute of Educational Informatics, Federal Research Center, Computer Science and Control of the RAS 44, block 2, Vavilov Str., Moscow 119333, Russia

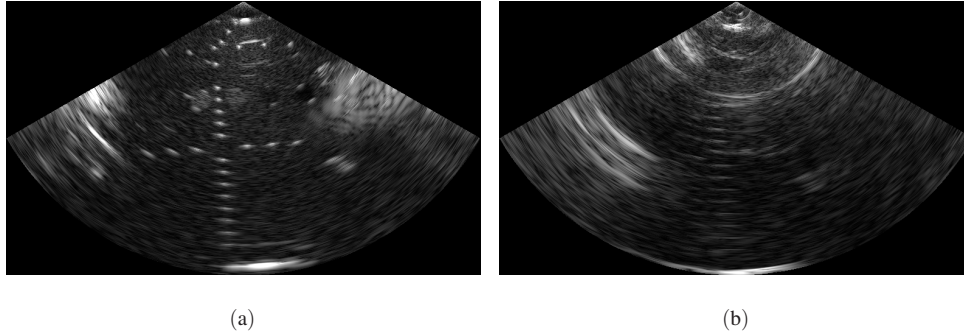(a)   (b)

Figure 1. Aberrations during the examination of Gammex 1430 LE phantom [8] by ultrasound scanner Sonomed-500 [26] through the surface of complex shape: (a) transducer data without the obstacle, (b) transducer data through the obstacle.

Correct diagnostics of vascular pathologies underlies treatment success in patients with cerebrovascular diseases. Transcranial ultrasound, namely transcranial Doppler (TCD) ultrasound, is the well-known, safe, non-invasive method with high sensitivity and specificity for diagnostics of cerebrovascular diseases [22, 25]. This method utilizes input signals of frequencies 1.8–2.5 MHz and allows us to estimate blood flow velocity in the major cerebral arteries.

TCD ultrasound examinations may be performed in two ways. The first method (duplex test) uses the B-mode ultrasound probe to visualize the structure of the head and Doppler ultrasound probe to estimate blood flow velocities. The second method uses only Doppler ultrasound probe, and obtained results entirely depend upon clinician's proficiency to detect correct vessels. Depending on insonated cerebral artery, ultrasound test can be done through four acoustic windows: temporal, orbital, suboccipital, and submandibular. The most effective transcranial ultrasound test in terms of viewing angle is the examination through the transtemporal window.

TCD test has some limitations, and here we specify the most essential of them in case of the duplex test. First and foremost, those are skull-induced signal aberrations which greatly depend on the patient-specific ultrasound permeability of temporal bone and its shape. The typical form of such aberrations is presented in Fig. for tissue phantom examination through a surface of complex shape. During the procedure the position of the transducer is not changed, but the presence of an uneven surface leads to a twisted, shifted and multiplied B-mode image.

It is quite often that images of brain major arteries are fragmented or the clinician can not get a clear picture of merging vertebral arteries. Sometimes the estimated direction of blood flow does not correspond to reality. Also, certain problems are associated with ultrasound transducer, they are listed in section 1.2.

Overcoming specified limitations of TCD test enables us to enhance the quality of diagnostics and to facilitate to development of new diagnostic methods (e.g. detection of small cerebral aneurysms).

Mathematical modelling can be applied to solve the problems mentioned above. In particular, numerical simulation of TCD ultrasound test can be used for elaboration of phase and amplitude aberration correction techniques which improve sig-

nificantly the quality of the B-mode images. The simulation of the TCD procedure with model parameters varied in a wide range helps to improve the understanding of the occurring processes and explain the causes of artifacts and noise. It allows us to develop algorithms which eliminate aberrations during automatic image processing. Such image processing may increase significantly the reliability of the transcranial ultrasound examination, reducing the human factor.

Thus, development of a sufficiently accurate transcranial ultrasound mathematical model is of prime importance, and the purpose of the current study is to develop such model.

Many publications address the numerical study of acoustic wave propagation in different media, we will mention only papers focused on simulation of ultrasound propagation in human tissues. Narasimhan *et al.* [17] considered acoustic problem for model of human thorax based on segmentation of CT scan images from Visible Human male data set, but they did not take into account the attenuation of waves in soft tissues. Ultrasonic wave propagation in human chest wall in two-dimensional formulation was considered by Mast *et al.* [16], where absorption effects were incorporated. Simulation of ultrasound propagation through the human breast are presented in [24]. Evaluating ultrasound interaction with bones is the essential part for different therapeutic and diagnostic applications (e.g. healing of bone fractures, assessment of osteoporosis), and the modalities in which ultrasound interacts with bone and soft tissues vary. Thus, ultrasound wave propagation in bones is a special topic of research [12].

To the authors knowledge, only few studies were related to transcranial ultrasound, and all of them considered numerical simulation of transcranial focused ultrasound (tFUS) [4, 14]. The tFUS is a non-invasive method for coagulation of a brain tumour due to increasing temperature in the tumour. The tFUS simulation produces the temperature and pressure fields within the skull and brain. The main aim of the articles on tFUS is the capability to predict and avoid unwanted secondary effects during the procedure and to estimate skull-induced aberrations which can lead to significant decrease in the treatment focal and thermal gain.

Similarly to tFUS, our work aims at optimization of transcranial ultrasound technique, but in different ways. It utilizes different frequencies and different signal inputs and analyses the obtained results in terms of the B-mode image processing. In addition, the TCD test simulation will assist to interpret ultrasound signals that have propagated through blood vessels with abnormalities to develop new diagnostic methods.

The present work is a proof of concept for the study of transcranial diagnostic ultrasound by numerical simulation tools. First, we are going to verify our numerical model in cases of human tissues phantoms, and then we will use a real human head anatomy for numerical experiments. In the solution of the system of equations for mechanics of deformable solids or acoustics, finite difference time-stepping and finite element method for spatial resolution are conventional. We use a grid-characteristic numerical method to solve the acoustic problem ([1, 18]). This approach takes into account specific features of hyperbolic equations and allows us

to achieve high accuracy for wave solutions in heterogeneous media.

The structure of this paper is as follows. In Section 1 we present governing equations for wave propagation problems neglecting all thermal effects. We also outline the operating principle of transducers and the B-mode image formation. The results of numerical experiments for acoustic problems in cases of phantom and human heads are presented and discussed in Section 2. Section 3 contains a few closing remarks.

1. Ultrasound propagation model

1.1. Governing equations and discretization

The studies of propagation of transverse (shear) and longitudinal (pressure) waves in human soft tissues show that the attenuation coefficient for shear waves is four orders of magnitude greater than that for pressure waves at MHz frequencies [7,15]. Therefore, human tissues are commonly treated as fluid in ultrasound imaging. We include longitudinal attenuation effects in our model using Maxwell solid model [16]. Equations of ultrasound propagation in human tissues have the following form:

$$\rho(\mathbf{x}) \frac{\partial \mathbf{v}(\mathbf{x},t)}{\partial t} + \nabla p(\mathbf{x},t) = 0 \qquad \text{in } \Omega$$

$$\frac{\partial p(\mathbf{x},t)}{\partial t} + \rho(\mathbf{x}) c^2(\mathbf{x}) \nabla \cdot \mathbf{v}(\mathbf{x},t) = -\alpha(\mathbf{x}) c(\mathbf{x}) p(\mathbf{x},t) \quad \text{in } \Omega \tag{1.1}$$

where Ω is the domain occupied by the tissues, $\mathbf{x}$ is a point in Ω, $\rho(\mathbf{x})$ is the density, $\mathbf{v}(\mathbf{x},t)$ is the velocity vector, $p(\mathbf{x},t)$ is the acoustic pressure, $c(\mathbf{x})$ is the speed of sound, $\alpha(\mathbf{x})$ is the attenuation coefficient. We assume that $\rho(\mathbf{x})$, $c(\mathbf{x})$, and $\alpha(\mathbf{x})$ are piecewise constant positive functions characterizing each tissue.

In this work two types of boundary conditions for (1.1) are used. The first one is an external force p^* acting on a part of medium boundary $\partial \Omega_f$

$$p|_{\partial \Omega_f} = p^*.$$

Zero external force ($p^* = 0$) means a free boundary. The second type of boundary condition is an absorbing boundary condition which will be presented later.

Equations of motion and rheological relations (1.1) in the Cartesian coordinate system (x_1, x_2, x_3) can be rewritten in a matrix form:

$$\frac{\partial \mathbf{u}}{\partial t} + \mathbb{A}_{x_1} \frac{\partial \mathbf{u}}{\partial x_1} + \mathbb{A}_{x_2} \frac{\partial \mathbf{u}}{\partial x_2} + \mathbb{A}_{x_3} \frac{\partial \mathbf{u}}{\partial x_3} = \mathbb{C}\mathbf{u} \tag{1.2}$$

where $\mathbf{u} = (v_1, v_2, v_3, p)^T$ is the vector of variables, v_i is the ith component of the velocity $\mathbf{v}$, $\mathbb{A}_{x_1}$, $\mathbb{A}_{x_2}$, $\mathbb{A}_{x_3}$, $\mathbb{C}$ are matrices of the 4th order.

The grid-characteristic method [1] is used for numerical solution of the system of hyperbolic equations (1.2). The system is solved by fractional time steps, at each

sub-step one solves the system of one-dimensional hyperbolic equations

$$\frac{\partial \mathbf{u}}{\partial t} + \mathbb{A}_{x_i} \frac{\partial \mathbf{u}}{\partial x_i} = 0 \tag{1.3}$$

and the system of ordinary differential equations responsible for dissipation

$$\frac{\partial \mathbf{u}}{\partial t} = \mathbb{C}\mathbf{u}. \tag{1.4}$$

The approximate solution of (1.3) and (1.4) at the nth time step is sought as a grid function with values $\mathbf{u}_m^n$ collocated in the mesh nodes and mesh mid-edges.

The spectral decomposition $\mathbb{A}_{x_i} = \mathbb{B}_i^{-1} \Lambda \mathbb{B}_i$, $\Lambda = \mathrm{diag}\{\lambda_1, \lambda_2, \lambda_3\}$, and introduction of Riemann invariants $\mathbf{r} = \mathbb{B}_i \mathbf{u}$ reduce (1.3) to the equation along characteristic curves Γ for each component r_j of $\mathbf{r}$:

$$\frac{\mathrm{d}r_j}{\mathrm{d}t} = 0 \tag{1.5}$$

where characteristic curves Γ are defined by

$$\frac{\mathrm{d}x_i}{\mathrm{d}t} = \lambda_j. \tag{1.6}$$

The values of $\mathbf{u}_m^{n+1}$ at the $(n+1)$th time layer and at the nth time layer are the same along these curves.

The grid-characteristic method for computing $\mathbf{u}_m^{n+1}$ at the point $\mathbf{x}_m^n$ solves (1.4) numerically and performs sequentially the steps for $i = 1, 2, 3$:

1. Compute eigenvalues λ_j for the matrix $\mathbb{A}_{x_i}$ and corresponding characteristic curves Γ_j using (1.6).

2. For each characteristic curve Γ_j find the point $\mathbf{x}_{j*}^n$ on intersection of Γ_j with time layer t^n.

3. Define $\mathbf{u}_{j*}^n$ in $\mathbf{x}_{j*}^n$ by quadratic interpolation in mesh tetrahedron containing $\mathbf{x}_{j*}^n$ and slope limiting as described in [18].

4. Compute the jth Riemann invariant r_{j*}^n at the point $\mathbf{x}_{j*}^n$ using the values $\mathbf{u}_{j*}^n$. This invariant is transferred along Γ_j to the point $\mathbf{x}_m^n$: $r_{jm}^{n+1} = r_{j*}^n$. Define $\mathbf{r}_m^{n+1}$ from components r_{jm}^{n+1}.

5. Find the values $\mathbf{u}_m^{n+1}$
$$\mathbf{u}_m^{n+1} = \mathbb{B}^{-1} \mathbf{r}_m^{n+1}.$$

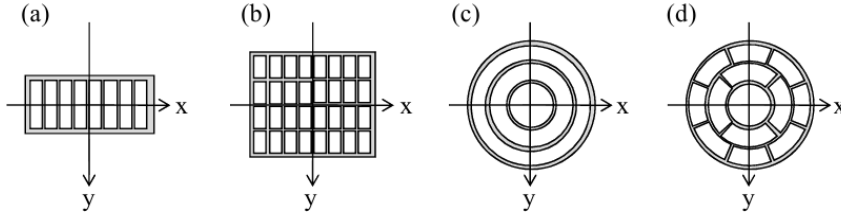(a)   (b)   (c)   (d)

Figure 2. The basic configurations of a phased array: (a) linear array, (b) matrix array, (c) annular array, (d) matrix array (sectored rings).

Figure 3. Example of raw transducer data. Each pixel row corresponds to a beam. Area on the left is closer to the sensor.

The computational mesh is Lagrangian: the mesh nodes are updated at each time step:

$$\mathbf{x}_m^{n+1} = \mathbf{x}_m^n + \Delta t \mathbf{v}_m^{n+1}. \tag{1.7}$$

The positions of mesh mid-edges are recalculated by averaging the positions of edge endpoints.

Propagating the grid functions along the characteristic curves is the fundamental of the grid-characteristic method. Implementation of the absorbing boundary condition is trivial in this framework: if a characteristic curve leaves the computational domain in a boundary node, then the corresponding Riemann invariant value is set to zero, $r_j = 0$. In case of transcranial ultrasound simulation, the absorbing boundary condition saves a lot of computing time: only the head and the neck interact with ultrasound and the remaining part of the human body lower the neck is neglected in simulation.

1.2. Operating principle of transducer and the B-mode image formation

Clinicians usually perform TCD ultrasound examination by phased array transducers [10]. Such transducer contains a set of several piezoelectric elements, which arrangement focuses the ultrasound beam at different planes. Figure 2 presents basic configurations of a phased array.

The elements of a phased array have a similar structure and are composed of a piezoelectric crystal (PZT, lead zirconate titanate), a backing layer and an acoustic matching layer. The piezoelectric element generates and receives the ultrasonic pulses. The backing layer is located behind the PZT element and is necessary to damp excessive vibration of the PZT element. As a result, the pulse length is shorten and the axial resolution of images is improved. The contrast of acoustic densities between the PZT element and soft tissues of a human body (the object) significantly decreases the transmission of the ultrasonic beam. In order to avoid this decrease,

one inserts an acoustic matching layer between the object and the PZT. The layer has intermediate acoustic properties and reduces the reflection of ultrasonic waves, increasing the energy transported by the ultrasonic beam up to 100%.

The piezoelectric elements can transmit and receive signals independently. Thus, using transmission delay laws for piezoelectric elements, we can construct a signal front of arbitrary shape, focusing ultrasonic beam at a specified location [21]. Focusing increases the wave amplitude at the region of interest and improves quality of the ultrasound image. It should be noted that there must be a recording delay for correct analysis of received signals. Namely, the first transmitting a signal element must be the last recording response with the delay of the last transmitting element.

Signals from all the elements with corresponding delays are collected on the analog level. Thus, the collected signal represents a generalized pressure on the whole sensor. One measurement gives us one row of pixels. The next measurement starts immediately after receiving the recordings. The focus is shifted along the region of interest and the sensor starts the new transmission. After the scanning of all the region we obtain a number of pixel rows that form a B-mode image. An example of raw data from the transducer is presented in Fig. 3.

The signal is postprocessed to reduce the noise and artifacts both on analog and digital levels. The complexity of postprocessing algorithms depends on the particular device and varies from simple elimination of the carrier frequency to advanced image processing.

The internal multiple reflection caused by the difference in rheological properties of bones and soft tissues is one of the problems of ultrasound examination. This problem is particularly relevant to the modelling of the ultrasound propagation through a human head. The difference in rheological properties of bones and soft tissues results in both aberrations due to passing through the structure of irregular form and multiple reflection from the bone surface. Lower wave dissipation rate in bones also leads to a high-amplitude noise lasting through several measurements and almost unpredictably changing the sensor data.

1.3. Signal characteristics

In our numerical studies of ultrasound examination we use a transducer with a phased linear array of 64 elements. The transducer sizes are 1.5×2.0 cm. Operational frequencies range from 2 to 7.5 MHz, the restrictions are imposed by the size of the single element [28]. For the virtual transcranial ultrasound examination we use the frequency 3.5 MHz as the most future-oriented.

Each element of the phased array transmits the following signal

$$p^* = p_0 \exp^{i2\pi\nu t} \exp^{-t^2/2\tau} \tag{1.8}$$

where ν is the frequency, τ is the pulse width, p_0 is the maximal amplitude of the signal, the delay depends on the position in the array.

For the chosen frequency the pulse width is 0.1–1 μs. Recording begins immediately after the transmission and lasts $2z_{max}/c$ seconds, where z_{max} is the estimated

depth of the pulse penetration. In case of a human head $z_{\max} \approx 15$ cm (skull back-side). The element size is equal to one half of the wavelength.

We consider sectoral scanning [13]. This type of ultrasound scanning is usually used for the TCD test, since the acoustic windows in this case are small in comparison to the region of interest. For sectoral scanning we have the following settings. Angular resolution is given by $\lambda/(2D)$, where λ is the wavelength and D is the size of the aperture determined by the size of the temporal window and ranges between 8 and 10 mm. The scanning angle range is $\pm 30°$. Scanning can be carried out for 64 and 200 rays, in the present article we use 64 rays.

2. Numerical results

2.1. Verification on phantoms

Human tissue-mimicking phantoms are objects with well-documented geometrical and mechanical parameters. The phantoms are used to configure the ultrasonic transducers and to train specialists [3]. The bulk of the volume is an inhomogeneous substance with approximately uniform scattering and attenuation properties (usually, a transparent polymer with some mineral powder) with acoustic properties matched to the properties of human tissues in terms of sound speed, scattering intensity and attenuation coefficients. The phantoms can imitate the shape and behaviour of real objects, or they can be just a cube of homogeneous material with multiple reflectors inside to calibrate the instrument. The different types of inhomogeneities are embedded in the volume. There are several types of inhomogeneities modelling various situations that can occur during medical examination. Their given location and properties make use of phantom convenient for verification of our simulations.

In the present study we use the B-mode phantom component of the Gammex 1430 LE phantom which allows us to estimate both Doppler and B-mode ultrasound systems [8]. The Gammex 1430 LE phantom consists of human tissue mimicking gel, vessels, closely spaced pins, and grey scale targets. Technical characteristics of this instrument can be found in [8]. These types of targets embedded in the tissue mimicking phantom are ideal to measure image quality in such terms of the B-mode image quality indicators as the depth of penetration, the axial resolution, the distance accuracy, the lateral resolution, the dead zone. The measurements of the Gammex 1430 LE phantom were performed by ultrasound scanner Sonomed-500 [26].

To meet the purpose of the study, we have chosen two types of inhomogeneities for the verification: point reflectors and grey scale targets. Schematic representations of computational domains are shown in Fig. 4. The general grey background for the B-scans of phantoms is obtained by scattering microscopic particles which act as point reflectors in the bulk volume. Different concentrations of these particles lead to different shades in grey scale targets. The modelling of the background is a complex problem, however its ignoring does not influence on the estimate of resolution and distance accuracy of the B-image, and we omit it here. We note that grey scale targets demonstrate the same behaviour in terms of bright specular echoes as regions
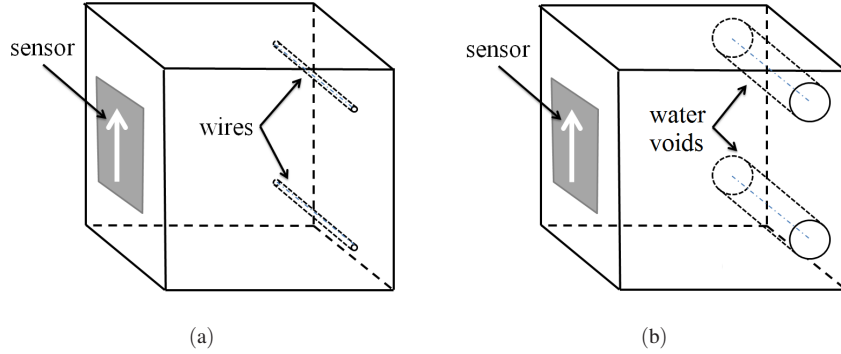
(a)   (b)

Figure 4. Schematic representations of computational area: (a) wires, (b) water voids.
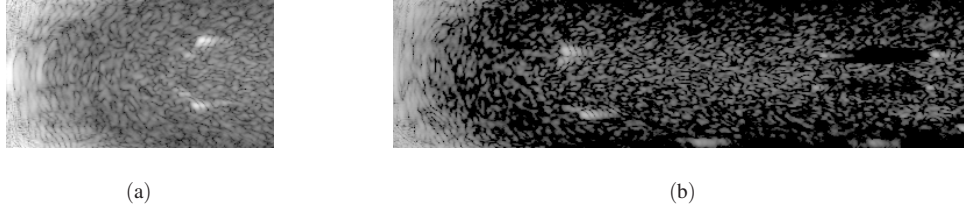

(a)   (b)

Figure 5. The B-mode images with analog signal processing obtained by ultrasound scanner Sonomed-500 for Gammex 1430 LE phantom: (a) wires, (b) water voids.
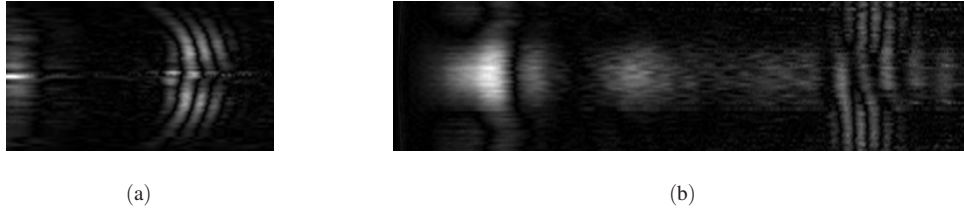

(a)   (b)

Figure 6. Simulation data: the raw B-scans without analog signal processing: (a) wires, (b) water voids.

with material parameters that differ from the bulk material, e.g. water. These echoes are considered artifacts but they are easier to obtain and they allow us to measure the distance between the modelled targets.

Point reflectors (Fig. 4a) are nylon wires of 0.1 mm^2 in cross section. We can see the point reflector response while the sensor is aligned perpendicularly to the wire direction and a line response if the sensor is aligned along the wire direction. The wires are located 16 mm under the phantom surface, the distance between the adjacent wires is 15 mm. Numerical resolution of such small object requires an extremely fine mesh (at least, locally) and the computing time is not reasonable in this case. We decided to model thicker wires with 0.5 mm^2 in cross section.

We consider the grey scale targets (Fig. 4b) as cylindrical water voids imitating vessels filled with blood. The grey scale targets are located 43 mm under the phantom surface, the distance between the adjacent voids is 19 mm, void radius is 4

Table 1.

Comparison of actual, experimental and simulation data: distance between targets, mm.

Type	Actual	Experiment	Simulation
Wires	15	15 ± 4	14 ± 8
Water voids	19	19 ± 4	20 ± 8

mm. By analogy with the wire inclusions, one observes specular echoes response for the sensor aligned orthogonally to the void direction and a line echo for the sensor aligned along the void direction, see Fig. 5.

In the numerical simulation, we use materials with properties given in Table 2. The transducer is modelled as an external force acting on the corresponding boundary patch, on the rest of the phantom boundary the absorbing boundary condition is imposed because the phantom boundaries are assumed to be far enough so that their acoustic response does not interact with the response from the targets. The results of the numerical simulation are presented in Fig. 6 where interference between signals from different targets at the middle pixel rows is shown. The algorithm of analog signal processing for the ultrasound scanner Sonomed-500 is not available and we can not reproduce the postprocessed B-mode image. We can compare only a limited number of image characteristics. One of these parameters is the distance between the targets. The comparison of the actual distances (the distances obtained with Sonomed-500 and with the simulation) is given in Table 1. The distances derived from the simulation B-scan images match the experimental and actual distances, but the possible errors of distance evaluations are large. The most appropriate evaluation of the simulation results is based on the pixel-by-pixel comparison of the B-mode image from Sonomed-500 and the postprocessed B-mode image from the simulation. Such comparison seems to be impossible without accurate formalization of the analog processing for Sonomed-500.

2.2. Virtual transcranial ultrasound

The segmented head model was obtained from the Computed Tomography Angiography (CTA) data of an anonymized 60 years old male patient. The original $512 \times 512 \times 501$ voxels dataset for the head and the torso top was cropped to the $262 \times 318 \times 353$ voxels dataset with voxel dimensions of $0.759 \times 0.759 \times 0.8$ mm. A conventional thresholding technique was used for bone segmentation. Brain, fat and muscle tissues were segmented by supervised random forest classification and active contour segmentation [29]. The blood vessels were segmented by the automatic segmentation technique for vascular structures [5]. Several post-processing steps were performed in order to improve the segmentation. The segmented head model is presented in Fig. 7. Insufficient CTA resolution prevents smaller vessels in the top half of the head from being resolved. However, the most important arteries are recovered successfully (carotid arteries, vertebral arteries, basilar artery, middle cerebral artery, the anterior cerebral artery, the posterior cerebral artery). Delaunay

Table 2.

Physical properties of tissues used in the simulation [6, 9, 11, 20, 27].

Tissue	ρ, kg/m^3	c, m/s	α, dB/cm
Phantom bulk material	1000	1540	4.02
Water	1000	1540	—
Nylon	1140	2290	—
Fat	916	1435	3.82
Muscle	1041	1595	6.21
Brain	1030	1550	4.34
Bone	1904	2031	25.75
Vessels	1066	1616	4.18

triangulation algorithm from CGAL Mesh library [23] was used to generate an adaptive unstructured tetrahedral mesh. The maximum element size is 2.4 mm, the minimum element size in the vicinity of the blood vessels and bones is 1 mm. The final mesh contains 108 076 tetrahedra and 29 656 vertices.

All the boundaries are considered to be free except for the boundary where the domain is truncated (human body below neck). The absorbing boundary condition is imposed on this boundary. Densities and sound speeds for considered tissues at the chosen frequency are presented in Table 2.

To demonstrate the impact of different speeds of wave propagation in different tissues, in Fig. 8 we present the pressure field patterns in the skull and the brain at different time instants. The figure shows that though the wave propagation speed in bone is higher than one in the brain, the wave fronts reach the back side of the skull simultaneously due to the convex shape of the skull. This may generate a higher response from the back side of skull. Individual features such as skull shape and bone tissue rheology parameters may intensify the response and cause measurement failure. If the depth of ultrasound scanning is adjusted to the center of the brain, the back side of the skull response will affect transducer data during the next measurement (the next transmitted ultrasonic beam) with an excessive noise. Increasing the scanning depth helps the response waves to reach the sensor during the same measurement, allowing us to distinguish the noise and separate it from useful data. Therefore, the transcranial ultrasonography should be performed at the maximum scanning depth.

In Fig. 9 we show the pressure fields at time moments $t_1 = 12.5\ \mu$s, $t_2 = 25.0\ \mu$s, $t_3 = 37.5\ \mu$s, $t_4 = 50.0\ \mu$s. The time $t = 0$ is the beginning of the scanning pulse. The wave attenuation is noticeable at distances about 7.5 cm. Due to small differences in averaged densities and speeds of sound for the brain and vessels tissues, the impact of the blood vessels to the pressure amplitude is minor. Nevertheless, the pressure exposed on the cerebral arteries distinguishes the arteries essentially (see Fig. 10). The maximal pressure exposed on a vessel is the measure of vessel visibility during the TCD examination. The maximal pressure (observed in simulation) on blood vessels varies significantly as well (see Fig. 11). Figure 11 demonstrates that the orbital and middle cerebral arteries are the most visible ones in the mode reproduced within simulation.
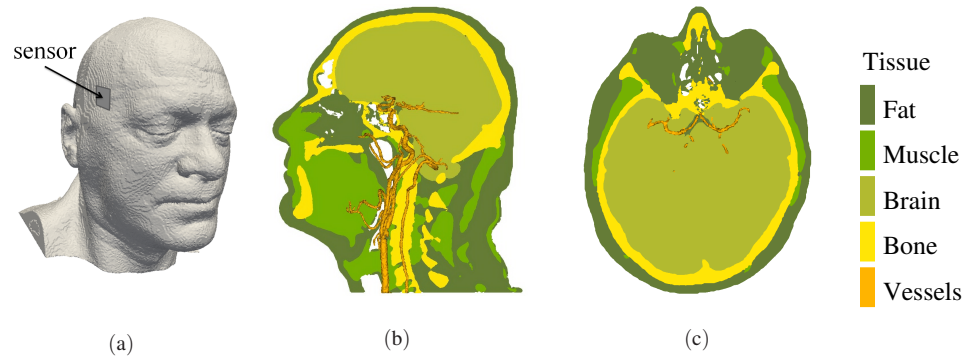
Figure 7. The segmented model: (a) general view with sensor indicated, (b) sagittal cut, (c) transverse cut.
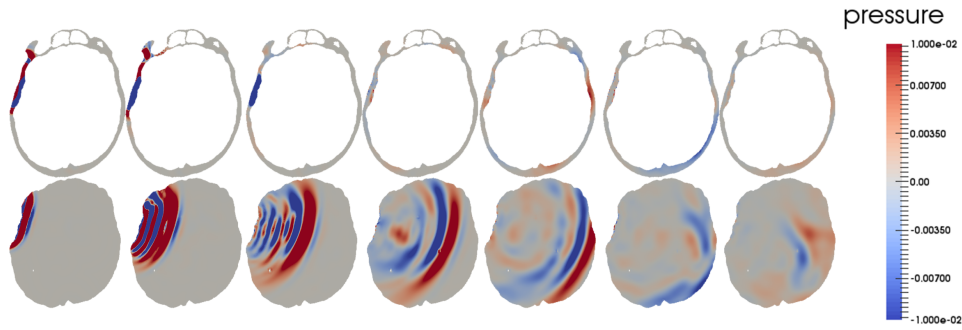

Figure 8. Wave patterns during the calculation (pressure field) for bone tissue (top) and brain tissue (bottom). Pressure units are kPa.
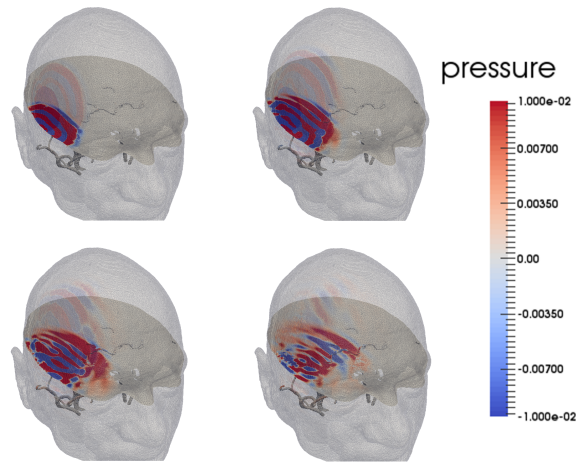

Figure 9. 3D wave pressure patterns at $t_1 = 12.5\ \mu$s (top left), $t_2 = 25.0\ \mu$s (top right), $t_3 = 37.5\ \mu$s (bottom left) and $t_4 = 50.0\ \mu$s (bottom right) after initiation of the scanning pulse. Pressure units are kPa.
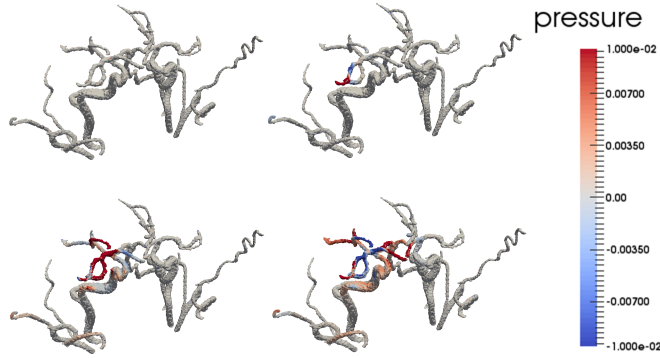
Figure 10. Pressure exposed on the cerebral arteries at $t_1 = 12.5$ μs (top left), $t_2 = 25.0$ μs (top right), $t_3 = 37.5$ μs (bottom left) and $t_4 = 50.0$ μs (bottom right) after initiation of the scanning pulse. Pressure units are kPa.
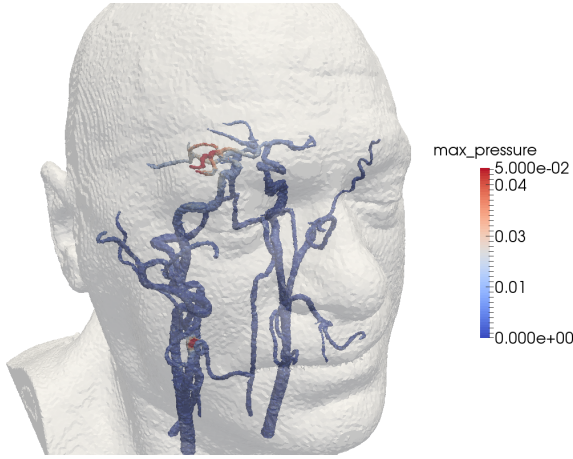

Figure 11. Maximal pressure observed on the cerebral blood vessels. Pressure units are kPa.

3. Conclusions

The present study is devoted to numerical simulation of ultrasound propagation in a human head by the grid-characteristic method. We used the B-mode component of the Gammex 1430 LE phantom to verify our numerical model in terms of the B-mode image quality. The simulation data match the actual data in terms of the distance between the targets. However, the numerical image can not be compared with the B-mode image produced by the scanner since the formalization of Sonomed-500 signal processing is lacking. Also, we computed pressure distributions within the 3D segmented model of a human head. Due to small differences in averaged densities and speeds of sound for the brain and vessels tissues, the impact of the blood vessels to the pressure field is minor. However, the pressure exposed on cerebral blood vessels varies significantly, and the maximal pressure is the measure of vessel visibility during the TCD examination.

There are several limitations in the presented model of ultrasound examination. First of all, for the sake of computational cost reduction we have considered vessels as an isotropic medium without blood. However, it is crucial to take into account moving blood in the TCD simulations. Considering bones as elastic solids and accounting shear wave propagation [27] may be important, as well. We did not compare the B-scan image obtained by the numerical model with the instrumental B-scan image because of lack of knowledge on image processing procedures implemented in ultrasound scanner software. The future work will address these issues. Nevertheless, the simulation results demonstrate that mathematical modelling of transcranial ultrasound can be an effective tool to enhance ultrasound examination.

Acknowledgements

References

1. K. A. Beklemysheva, A. A. Danilov, I. B. Petrov, V. Yu. Salamatova, Yu. V. Vassilevski, and A. V. Vasyukov, Virtual blunt injury of human thorax: Age-dependent response of vascular system. *Russ. J. Numer. Anal. Math. Modelling* (2015) **30**, No. 5, 259-268.

2. J. Bushberg, J. Seibert, E. Leidholdt Jr., and J. Boone, *The essential physics of medical imaging*, Lippincott Williams & Wilkins, 2011.

3. Catalog of human tissues phantoms. URL: http://doza.ru/catalog/ultrasound_training_phantoms.

4. C. W. Connor, and K. Hynynen, Patterns of thermal deposition in the skull during transcranial focused ultrasound surgery. *IEEE Trans. Biomed. Engrg.* (2004) **51**, No. 10, 1693-1706.

5. A. Danilov, Y. Ivanov, R. Pryamonosov, and Y. Vassilevski, Methods of graph network reconstruction in personalized medicine. *Int. J. Numer. Method Biomed. Engrg.* (2015) **32**, No. 8, e02754.

6. F.A. Duck, *Physical Properties of Tissue*, Academic Press, London, 1990.

7. L. A. Frizzell, E. L. Carstensen, and J. F. Dyro, Shear properties of mammalian tissues at low megahertz frequencies. *J. Acoust. Soc. Amer.* (1976) **60**, No. 6, 1409–1411.

8. Gammex 1430 LE phantom. URL: http://cspmedical.com/content/102-1880_mini_doppler_brochure.pdf.

9. S. A. Goss, R. L. Johnston, and F. Dunn, Comprehensive compilation of empirical ultrasonic properties of mammalian tissues. *J. Acoust. Soc. Amer.* (1978) **64**, No. 2, 423–457.

10. C. R. Hill, Generation and structure of acoustic field. In: *Physical Principles of Medical Ultrasonics* (Eds. C. R. Hill, J. C. Bamber, and G. R. ter Haar). John Wiley & Sons, Chichester, 2004, pp.41-68.

11. P. R. Hoskins, Physical properties of tissues relevant to arterial ultrasound imaging and blood velocity measurement. *Ultrasound Med. Biol.* (2007) **33**, No. 10, 1527–1539.

12. J. J. Kaufman, G. Luo, and R. S. Siffert, Ultrasound simulation in bone. *IEEE Trans. Ultrason. Ferroelectr. Freq. Control.* (2008) **55**, No. 6, 1205–1218.

13. N. Kazuyuki, and K. Naoyuki, 3-D Modellings of an ultrasonic phased array transducer and its radiation properties in solid. In: *Ultrasonic Waves*. (Ed. A. Santos). Intech, 2012, pp. 59–80.

14. A. Kyriakou, E. Neufeld, B. Werner, G. Székely, and N. Kuster, Full-wave acoustic and thermal modelling of transcranial ultrasound propagation and investigation of skull-induced aberration correction techniques: a feasibility study. *J. Ther. Ultrasound.* (2015) No. 1, 1–48.

15. E. L. Madsen, H. J. Sathoff, and J. A. Zagzebski, Ultrasonic shear wave properties of soft tissues and tissuelike materials. *J. Acoust. Soc. Amer.* (1983) **74**, No. 5, 1346–1355.

16. T. D. Mast, L. M. Hinkelman, L. A. Metlay, M. J. Orr, and R. C. Waag, Simulation of ultrasonic pulse propagation, distortion, and attenuation in the human chest wall. *J. Acoust. Soc. Am.* (1999) **106**, No. 6, 3665-3677.

17. C. Narasimhan, R. Ward, K. L. Kruse, M. Guddati, and G. Mahinthakumar, A high resolution computer model for sound propagation in the human thorax based on the Visible Human data set. *Comput. Biol. Med.* (2004) **34**, No. 2, 177–192.

18. I. B. Petrov, A. V. Favorskaya, A. V. Shevtsov, A. V. Vasyukov, A. P. Potapov, and A. S. Ermakov, Combined grid characteristic method for the numerical solution of three dimensional dynamical elastoplastic problems. *Comput. Math. Math. Phys.* **54** (2014), No. 7, 1176–1189.

19. I. B. Petrov, A. V. Vasyukov, K. A. Beklemysheva, A. S. Ermakov, A. S. Dzuba, and V. I. Golovan, Numerical modelling of low energy strike at composite stringer panel. *Matem. Modelir.* **26** (2014), No. 9, 96–110. (in Russian).

20. S. Pichardo, V. W. Sin, and K. Hynynen, Multi-frequency characterization of the speed of sound and attenuation coefficient for longitudinal transmission of freshly excised human skulls. *Phys. Med. Biol.* **56** (2011), No. 1, 219–250.

21. J. Powers and F. Kremkau, Medical ultrasound systems. *Interface focus* **1** (2011), No. 4, 477–489.

22. K. Rajamani and M. Gorman, Trancranial Doppler in stroke. *Biomed. Pharmacother.* **55** (2001), No. 5, 247–257.

23. L. Rineau and M. Yvinec, A generic software design for Delaunay refinement meshing. *Computational Geometry* **38** (2007), 100–110.

24. G. Salahura, J. C. Tillett, L. A. Metlay, and R. C. Waag, Large-scale propagation of ultrasound in a 3-D breast model based on high-resolution MRI data. *IEEE Trans. Biomed. Engrg.* **57** (2010), No. 6, 1273–1284.

25. S. Sarkar, S. Ghosh, S. K. Ghosh, and A. Collier, Role of transcranial Doppler ultrasonography in stroke. *Postgrad. Med. J.* **83** (2007), No. 985, 683–689.

26. Ultrasound scanner Sonomed-500. URL: http://spectromed.com/en.

27. P. J. White, G. T. Clement, and K. Hynynen, Longitudinal and shear mode ultrasound propagation in human skull bone. *Ultrasound Med. Biol.* **32** (2006), No. 7, 1085–1096.

28. T. Whittingham and K. Martin, Transducers and beam forming. In: *Diagnostic Ultrasound Physics and Equipment* (Eds. P. R. Hoskins, K. Martin, A. Thrush). Cambridge University Press, 2010 pp. 23–46.

29. P. A. Yushkevich, J. Piven, H. C. Hazlett, R. G. Smith, S. Ho, J. C. Gee, and G. Gerig, User-guided 3D active contour segmentation of anatomical structures: significantly improved efficiency and reliability. *Neuroimage* **31** (2006), No. 3, 1116–1128.